Composites: Part A 185 (2024) 108271

Contents lists available at ScienceDirect

Composites Part A

journal homepage: www.elsevier.com/locate/compositesa

Unraveling chemical and rheological mechanisms of self-healing with EMAA thermoplastics in fiber-reinforced epoxy composites

Alexander D. Snyder [a], Jack S. Turicek [a], Charles E. Diesendruck [b], Russell J. Varley [c], Jason F. Patrick [a,d,*]

[a] Department of Mechanical and Aerospace Engineering, North Carolina State University, Raleigh, 27695, NC, USA
[b] Schulich Faculty of Chemistry, Technion - Israel Institute of Technology, Haifa, 3200003, Israel
[c] Institute for Frontier Materials, Deakin University, Geelong Waurn Ponds, 3216, Victoria, Australia
[d] Department of Civil, Construction, and Environmental Engineering, North Carolina State University, Raleigh, 27695, NC, USA

ARTICLE INFO

In memory of Adrian P. Mouritz, former Professor and Dean of Engineering at the Royal Melbourne Institute of Technology (RMIT), and a pioneer in self-healing fiber-composites using EMAA.

Keywords:
A. Fracture
B. Delamination
C. Self-healing
D. Multifunctional

ABSTRACT

Interlaminar delamination is a prevalent and insidious damage mode limiting the mechanical integrity and lifetime of fiber-reinforced composites. Conventional resolution involves over-design, laborious inspection, and repair/replacement at cost to the economy and environment. Self-healing via *in situ* thermal remending of thermoplastic interlayers offers a promising solution. However, better understanding of the healing agent and related mechanisms is necessary to tailor healing performance. Here, we compare non-neutralized (copolymer) and metallic-ion neutralized (ionomer) poly(ethylene-co-methacrylic acid) (EMAA) thermoplastics for healing interlaminar fracture. We reveal (i) how EMAA chemistry affects the interfacial reactions driving healing and (ii) the influence of molten viscosity on repair efficiency. At fixed viscosity, higher methacrylic acid content, chain mobility, and lower neutralization positively influence healing, where lower melt viscosity at fixed temperature improves delamination recovery. Thus, this study deepens scientific understanding of key variables for healing interlaminar fracture with EMAA, providing new insight for the design of multifunctional composites.

1. Introduction

Fiber-reinforced polymer (FRP) composites are ubiquitous structural materials possessing high specific stiffness and strength owing to their hierarchical arrangement. However, this makeup renders susceptibility to multiscale damage, ranging from micro-cracks that are millimeters in length to interconnected fractures spanning several centimeters [1,2]. Interlaminar delamination (i.e., debonding of the fiber–matrix interface) is especially prevalent in FRP due to the general lack of through-thickness reinforcement and can significantly limit the service lifetime and reliability of lightweight structures. Modern structural health monitoring (SHM) and non-destructive evaluation (NDE) techniques demonstrate mixed success locating often subsurface delamination damage [1,3], whereas repair is also difficult and often mandates the replacement of affected components [4,5]. If undetected and unaddressed, delamination jeopardizes FRP mechanical integrity and increases the risk of catastrophic failure [6,7]. Delamination can be mitigated via stitching [8], weaving [9], or Z-pinning [10] to bind reinforcing plies together, though often with penalty to in-plane mechanical properties due to induced fiber waviness [11]. Over-design and life-limiting design strategies are more common for delamination mitigation [6,12,13], though such techniques often result in bulky structures and are less sustainable due to FRP thermoset matrices largely being non-recyclable [14]. Next-generation FRP composite structures aim to offset such drawbacks via new design paradigms, for example self-healing of recurrent damage modes [15].

Self-healing has proven viable in FRP composites via *extrinsic* approaches, (i.e., inclusion of non-native healing agents within host laminates). Capsule-based self-healing systems comprising liquid filled capsules that autonomously rupture to enable payload polymerization in the presence of a reactive agent have demonstrated success in restoring matrix damage [16,17]. However, micro-capsules only function for a single damage-heal cycle and remedy small (micron scale) crack separations [18–21]. Vascular self-healing strategies have emerged to overcome such limitations, enabling multiple healing cycles and restoring larger crack separations while increasing resistance to fracture [22,23] and allowing tailored design of vesicle structure [24]. Upon delamination, vesicles rupture and deliver sequestered healing agents to the damaged region either via passive transport (i.e., capillary flow) or

* Corresponding author at: Department of Civil, Construction, and Environmental Engineering, North Carolina State University, Raleigh, 27695, NC, USA.
E-mail address: jfpatric@ncsu.edu (J.F. Patrick).

https://doi.org/10.1016/j.compositesa.2024.108271
Received 24 February 2024; Received in revised form 22 April 2024; Accepted 14 May 2024
Available online 22 May 2024

active pumping, with subsequent healing via diffusion-dominated polymerization reactions. To date, widespread adoption of such technology is limited by challenges in achieving stoichiometric mixing *in situ*, cross-contamination or vascular blockages by healed material, and limited stability of chemical agents in variable service environments [15,25].

Imbuing FRP with *intrinsic* self-healing capability, reliant on chemical bond reassociation in the host material, can avoid aforementioned limitations while enabling repeatable fracture surface rebonding and significant lifetime extension [26,27]. Energetic barriers for rebonding (i.e., healing) can be overcome via application of various stimuli such as light, heat, and pressure [28]. While successful in both soft, flexible [29], and also rigid, structural polymers [30], well-explored intrinsic self-healing strategies such as the use of reversible covalent Diels–Alder crosslinks [31] or specialized supramolecular healing chemistries have limited applicability in FRP due to healing temperatures above the matrix glass transition temperature (T_g) or inferior mechanical properties [32]. Novel self-healing structural matrices based on covalent adaptable networks (e.g., vitrimers), while promising, often require significant heat and pressure to heal delamination effectively [33]. Additionally, vitrimer transition temperatures (T_v) lie below their own glass transition and often lower than 100 °C, restricting operation below desired FRP service temperatures [33]. Alternatively, *hybrid* extrinsic–intrinsic approaches relying on the thermally-assisted melting, flow, and reassociation of remendable thermoplastic domains within the thermoset matrix (i.e., thermal remending) have demonstrated successful restoration of superficial indentations [34], flexural fatigue cracks [35], interlaminar fracture [36], and impact damage [37,38]. Poly(ethylene-co-methacrylic acid) (EMAA) thermoplastic is a particularly successful toughening and healing agent due to its unique ability to form interfacial covalent and ionic bonds with thermoset epoxies based on digicidyl ether of bisphenol A (DGEBA). Specifically, epoxide-EMAA carboxylic acid reactions occur concomitantly during epoxy-amine curing reactions, the former promoting excellent adhesion between the thermoplastic healant and thermoset matrix and increasing fracture toughness/delamination resistance [39]. The superior bonding restricts cracks to propagate through the tough thermoplastic (cohesively) as opposed to the EMAA-epoxy interface (adhesively) [40,41]. Another factor contributing to favorable healing is the well-documented thermally activated pressure delivery mechanism [40,42,43], which forces EMAA into confined cracks. This is first enabled by interfacial esterification/condensation reactions between the immiscible EMAA and epoxy hydroxyl groups formed during epoxy-amine curing. This EMAA/epoxy interfacial reaction is catalyzed by tertiary amines within the epoxy matrix, which are produced during the later stages of curing after the primary and secondary amines are consumed. Water vapor produced by these reactions coalesces into a separate phase within the EMAA. During healing, the composite is heated above the boiling point of water (100 °C) and the dormant moisture transforms into a gaseous phase, greatly expanding in volume. Since the EMAA is above its melting point of (≈ 80 °C), and with low enough melt viscosity, the pressurized water vapor directs the thermoplastic into any available space. The EMAA can thus spread along a fracture and into branching microcracks, producing a plethora of microporous cavities—further evidence of such interfacial condensation reactions during healing. Over repeated healing cycles, EMAA transforms from a microporous topology into a smooth film (conforming to the fracture surface) as covalent/ionic reactions wane and healing becomes largely dependent on hydrogen bonding and van der Waals interactions.

EMAA has been successfully deployed in particle [39,44,45], fiber [43], mesh [46], and Z-stitch [47,48] morphologies to enable self-healing of FRP damage *ex situ* (i.e., in an oven). Recent advances have demonstrated prolonged sub-T_g, *in situ* self-healing of interlaminar damage in both glass- and carbon-fiber composites via heat applied by embedded resistive heaters [40,49] and the evolution of EMAA/epoxy chemical reactions and maintenance of hydrogen bonding between adjoining EMAA domains. However, EMAA-based healing studies to date have largely focused on non-ionic copolymers whose properties rely on hydrogen bond formation between methacrylic acid clusters on the polymer backbone [50,51]. Ionomers of EMAA are readily created via salt neutralization of methacrylic acid groups, altering mechanical properties via tailoring ionic content, i.e., relative amounts of ionic cluster attraction and methacrylic acid cluster hydrogen bonding [50]. While increasing ionic content adversely affects low velocity ballistic self-healing of EMAA films due to increased viscosity that limits molten flow and perforation fusion [52], healing under high-velocity conditions remains promising even at high degrees of neutralization. This is attributed to greater frictional heating enabling molten flow without collapsing the perforated polymer film [53,54]. Tailoring of cluster behavior via carboxylic acid modification can also improve plastic flow and recovery speed, with elastic response controlled by neutralization [55]. Thus, vast potential exists for tailored healant development in consideration of polymer elastic properties, melt viscosity, and chemical reactivity. However, the evaluation of EMAA healants with varying physical and chemical properties has been largely unexplored for the repair of interlaminar delamination in FRP composites. Here we study the thermal remending capability of four EMAA variants–two Nucrel™ copolymers and two Surlyn™ ionomers–with differing chemical composition: Nucrel™ 2940 (19 wt% methacrylic acid) [56], Nucrel™ 960 (15 wt% methacrylic acid) [57], Surlyn™ 1702 (Zn^{2+}-neutralized ionomer) [58] and Surlyn™ PC-2200 (Na^{+}-neutralized ionomer) [59].

Fig. 1 depicts the associated mechanisms for thermal remending of interlaminar damage in our model epoxy-matrix glass-fiber composite material. Upon delamination, cohesive failure of 3D-printed EMAA domains occurs due to sufficient interfacial bonding between the thermoplastic and reinforcement/matrix phases. Post-fracture, *in situ* heating via electrical power input to embedded textile resistive heaters melts the cohesively fractured EMAA domains, whereby direct contact of the molten thermoplastic interfaces engenders repeated thermal remending. Various chemical and physical mechanisms contribute to the self-repair. ①: Strong interfacial bonding via mechanical interlock of EMAA with bundles of μm scale fibers and covalent interactions (I) between EMAA and the epoxy matrix which helps ensure repeatable cohesive failure of the EMAA domains; ②: A decrease in thermoplastic melt-viscosity enables spreading of the healing agent across the fracture surface to further increase the bonding area and enhance fracture recovery; ③: Within confined cracks, spreading is assisted via pressurization from the formation of water-vapor within the EMAA due to aforementioned condensation reactions between carboxylic acid in the EMAA and hydroxyl groups in the composite constituents (II), which is vaporized during *in situ* heating [42]; ④: This pressurization also assists with multi-scale crack filling of molten EMAA, which upon solidification, re-bonds to the fracture surface via non-covalent hydrogen and ionic bonds (III) [60].

Experimental investigation of these chemo-physical healing mechanisms is conducted in double cantilever beam (DCB) mode-I fracture specimens via two comparative studies: (1) a fixed healing temperature of 130 °C (variable melt viscosity) and (2) a fixed melt viscosity of 1528 Pa·s (variable healing temperature). In addition to quantifying fracture recovery, relevant topological and chemical phenomena are elucidated via scanning electron microscopy (SEM) and Fourier transform infrared spectroscopy (FTIR). Thus, we build key understanding of the EMAA thermal remending mechanisms in FRP composites and how the thermoplastic healing agent properties (physical and chemical) alter self-healing performance, thereby providing crucial knowledge for real-world translation.

2. Materials and methods

2.1. Additive manufacturing

2.1.1. Extrusion of EMAA filament feedstock

Thermoplastic filament with a diameter of ≈ 2.5 mm for fused deposition modeling (FDM) was produced from as-received pellets of

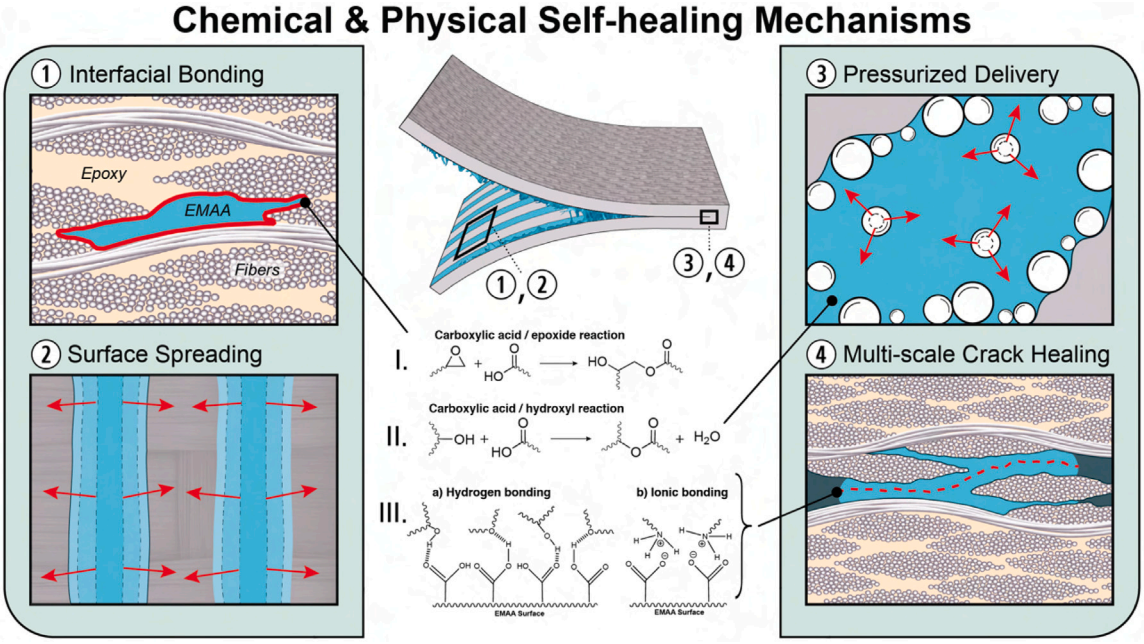

Fig. 1. Chemical and Physical Self-healing Mechanisms. Schematic depicting critical aspects of the thermally activated self-healing mechanisms in a glass fiber-reinforced composite (GFRP): ① Covalent EMAA-epoxide reaction (I) that helps provide a strong interfacial bond (in addition to mechanical interlock with fiber-reinforcement) to ensure cohesive failure through the EMAA for enhanced fracture toughness and repeated repair; ② Molten EMAA (> 80 °C) surface spreading where the flow is driven by physical/chemical processes to increase fracture surface coverage for greater recovery; ③ Pressurized delivery of molten thermoplastic resulting from EMAA-hydroxyl interfacial reactions (II) with the matrix and glass-fiber surfaces that produce water, which expands during healing at elevated temperature (> 100 °C) as the moisture is transformed into vapor, thereby directing viscous thermoplastic across free surfaces and into confined cracks; ④ Multi-scale (i.e., micro-crack and delamination) healing upon cooling and EMAA solidification that re-bonds fracture surfaces via non-covalent hydrogen and ionic bonding (III).

each EMAA variant (Dow Chemical, Inc.) using a twin-screw extruder (Haake Polylab OS, Thermo-Fisher Scientific, Inc.) with a 2 mm circular die. The co-rotating screw speed was kept at 100 RPM, with extrusion temperatures set to 120, 135, 190, and 170 °C for the Nucrel™ 2940, Nucrel™ 960, Surlyn™ PC-2200, and Surlyn™ 1702, respectively. Molten EMAA was cooled to room temperature (RT ≈ 23 °C) via post-extrusion transfer through a water bath and collected on a set of rotating steel rollers.

2.1.2. FDM patterning of E-glass substrates

Serpentine patterns of each EMAA variant were printed directly onto 8-harness satin (8HS) woven E-glass reinforcement (Style 7781, Hexcel, Inc.) using a TAZ Pro FDM 3D-printer (Lulzbot, Inc.) with a 500 μm diameter nozzle and 900 mm/min print head travel speed. The print nozzle and bed temperatures for all polymers were maintained at 190 and 65 °C, respectively. Continuous serpentine patterns, oriented with the primary traces parallel to the crack propagation direction (i.e., the fabric warp direction), were deposited at an areal coverage of 16 % relative to the substrate surface area (≈ 0.95 vol%) enabling increased fracture resistance and appreciable delamination recovery without causing fracture in adjacent (i.e., untoughened) interlayers [41]. Cross-sectional dimensions of the as-printed traces were maintained at ≈ 500 ± 50 μm wide and ≈ 310 ± 20 μm tall producing a steady fracture response consistent with prior work [41,49]. Following the melt-consolidation process described in Section 2.3.3, molten spreading of the thermoplastic results in flattening of EMAA cross-sections and nesting within neighboring fiber interfaces [41], though the serpentine profile is largely maintained.

2.2. Rheological characterization of EMAA variants

Parallel plate rheometry was performed on as-received pellets of each EMAA variant using a hybrid rheometer (TA Instruments, Inc.). The pellets were placed on the bottom platen at RT and held in place using a retaining ring while heated to an initial temperature of 100 °C and melt-consolidated into a monolithic film. The retaining ring was then removed and the top platen was brought into contact with the film while preserving a gap of 1 mm relative to the bottom platen. A shear rate of $\dot{\gamma} = 0.1\ s^{-1}$ was applied while the temperature was ramped at 1 °C/min from 100 to 200 °C (above all melt transitions).

2.3. Manufacture of self-healing composites

2.3.1. Internal electrical connections to resistive heaters

Two resistive heater textile plies (LaminaHeat, LLC), each 254 mm wide and 140 mm long, were placed into self-healing composite preforms. Prior to incorporation, each of these heater plies was marked along both continuous rows of conductive copper bus bars to delineate centerline locations of eight (25 mm wide) samples and for external electrical connections. A steel razor blade was used to perforate the top E-glass layer insulating the bus bars via a 15 mm long slit from the outer edges along the sample centerlines. The perforations were coated with conductive silver paint, which dried for 30 min before placing a 25 mm long segment of copper wire (0.81 mm diameter) into each slit (10 mm overhang) and subsequent application of a silver paint overcoat. After an additional 30 min of drying, the connected wires were potted with a thin layer of structural adhesive (DP460NS, 3M, Inc.), secured using a single layer of conductive copper tape, and cured at 49 °C for 4 h. Introducing resistive heater plies was previously shown to not significantly affect the in-plane tensile properties in glass-fiber composites [49].

2.3.2. Preform construction

Plain composite preforms (i.e., without EMAA augmentation) comprised sixteen 8HS woven plies in an alternating sequence of $[0/90]_8$, where 0° corresponds to the fabric warp direction and 90° the weft direction. Since the warp and weft fiber-counts are equal, rotating each successive ply by 90° (i.e., rotated pairs) minimizes coupling terms to produce a "quasi-symmetric" laminate [61]. Preforms for self-healing composites comprised two resistive heater plies and a middle ply

Table 1
Melt consolidation temperatures for composite preforms containing printed patterns of each EMAA variant.

EMAA variant	Melt consolidation temperature (°C)
Nucrel™ 2940	110
Nucrel™ 960	148
Surlyn™ PC-2200	168
Surlyn™ 1702	172

patterned with the chosen EMAA variant, and thirteen additional plies of E-glass in a stacking sequence of: $[0/90]_2$-heater-[0/90/0]-EMAA-[90/0/90]-heater-$[0/90]_2$. A 25 μm thick ethylene tetrafluoroethylene (ETFE) film (full panel width and 50 mm long) was placed atop the midlayer of each preform to serve as a pre-crack for subsequent fracture testing.

2.3.3. Melt-consolidation

Completed preforms (254 by 254 mm) were placed between a pair of aluminum plates (405 × 405 × 6.35 mm, width × length × thickness) and weighted to a total pressure of 1 kPa relative to the preform surface area. The preform/plate assembly was heated in a mechanical convection oven (OF-22, Cole-Parmer, Inc.) from room temperature (RT) to the target consolidation temperature (defined in Table 1) over a 15 min period. Consolidation temperatures were chosen to produce equivalent viscosity across all EMAA variants in the melted state. The consolidation temperature was held for 75 min and then reduced to 60 °C over a 90 min period prior to removal of the assembly from the oven. Upon removal, the melt-consolidated preform was then cooled to RT.

2.3.4. Vacuum assisted resin transfer molding (VARTM)

Prior to infusion of the composite preforms, epoxy resin and amine hardener (Araldite LY/Aradur 8615, Huntsman Advanced Materials, LLC) were mixed at 50 pph and degassed for 2 h at RT under 12 Torr abs vacuum within a vacuum drying oven (ADP 300C, Yamato, Inc.)

Vacuum infiltration of the degassed resin system into the preforms was conducted at 2 Torr (abs) until complete fabric wetting and then the vacuum was decreased to 380 Torr (abs) for 27 h at RT until matrix solidification. The infused composite panels were cured for 2 h at 121 °C followed by 3 h at 177 °C to yield a glass transition temperature $T_g \approx 196$ °C as measured by dynamic mechanical analysis (DMA).

2.3.5. Fracture specimen fabrication

After composite manufacturing, double cantilever beam (DCB) fracture specimens 25 mm wide and 140 mm long were cut from each ≈ 4 mm thick composite panel using a diamond-blade wet saw (41-AR, Sowers Dia-Met, Inc.). Steel hinges were bonded to the outer composite faces on the pre-crack end with structural adhesive and cured at RT for 24 h plus an additional 4 h at 49 °C to reach full strength in the adhesive. The DCB top face was spray painted matte black for infrared (IR) imaging. A line 50 mm from the interior edge of the pre-crack was delineated on the bottom and side faces to mark the termination point for delamination propagation during fracture testing.

2.3.6. External electrical connections to self-healing composites

Each DCB specimen featured four exposed cross-sections of embedded copper wire (0.81 mm diameter), two at each end. A central 0.65 mm diameter hole was drilled 4 mm into each embedded wire and another copper wire (0.64 mm diameter) was inserted into each hole. Potting of the connection was performed using a commodity two-part epoxy system with a 5 min working time (The Gorilla Glue Company, Inc.). A 24 h RT cure was then performed to obtain full strength in the potted connection [62].

2.4. Thermomechanical characterization of composite constituents

2.4.1. Sample fabrication

Neat epoxy samples (≈ 2.1 mm thick) were produced via cell casting between glass plates with a silicone rubber gasket and cured for 24 h at RT until resin solidification, followed by 2 h at 121 °C and 3 h at 177 °C. Plain composite samples (≈ 1.8 mm thick) comprised eight 2D woven plies in an alternating sequence of $[0/90]_4$. Preforms were infused via the VARTM process and cured at the same conditions as the cell castings. Both the neat epoxy and plain composite samples were cut to 10 mm wide and 60 mm long using a diamond-blade wet saw.

2.4.2. Dynamic mechanical analysis (DMA)

DMA was performed on neat epoxy and plain composite samples in 3-pt flexure (50 mm span length) according to ASTM E1640 [63]. A dynamic mechanical analyzer (Q800, TA Instruments, Inc.) applied an oscillating strain of 0.1% at 1 Hz frequency following an initial preload of 0.01 N. A temperature sweep from RT to 250 °C was conducted at a ramp rate of 5 °C/min with storage modulus (E′), loss modulus (E″), and $\tan(\delta)$ data collected at a sampling rate of 0.5 Hz. The peak of $\tan(\delta)$ was reported as the T_g for each sample.

2.5. Fracture testing and self-healing evaluation

Mode-I fracture testing of double cantilever beam (DCB) specimens was conducted in accordance with ASTM D5528 [64] and other prior works [65,66] using a 10 kN electromechanical load frame (Alliance RT/5, MTS, Inc.) equipped with a 250 N load cell. The initial pre-crack region (a_0) in each sample was ≈ 35 mm long and served to direct the propagating delamination along the sample midplane. A 4K resolution webcam (Logitech BRIO), equipped with a custom macro lens (LM12JC5M2, Kowa Optical Products Co., Ltd.) was mounted underneath the specimen in conjunction with necessary backlighting to accurately monitor crack front propagation (Fig. 2a). Samples were tested quasi-statically (i.e., continuous fracture propagation at a constant slow speed [67]) via displacement controlled loading at a rate of 5 mm/min to an incremental crack length (Δa) of 50 mm and subsequently unloaded (at the same rate) to the original zero crosshead displacement for all test cycles (Fig. 2b). *In situ* self-healing via thermal remending was performed within the load frame. Heating commenced via electrical power application to the resistive heater layers using a DC power supply (PWS4602, Tektronix, Inc.). Power was supplied for 15 min (10 min ramp, 5 min dwell) to achieve the desired maximum top surface temperature (Fig. 2c) for each healing condition (Table 2) as monitored by an overhead IR camera (A600, Teledyne FLIR, Inc.) before disconnecting power and allowing the specimen to cool for 30 min to RT. The healing conditions in Table 2 were chosen to enable melt flow of EMAA during thermal remending without exceeding the epoxy matrix glass transition temperature (T_g). Following cooling, specimens were reloaded (Fig. 2d) to assess self-healing efficiency. Representative cross-sections of composites in pristine, fractured, and healed states are shown in the Appendix A.3.

For all testing cycles, mode-I critical strain energy release rate (G_{IC} in Eq. (1))–a measure of crack-growth resistance–was calculated using the area method according to the expression [65]:

$$G_{IC} = \frac{1}{b}\frac{\Delta U}{\Delta a}, \tag{1}$$

where b is the sample width, Δa is the measured change in crack length, and ΔU is the change in internal work or strain energy due to elastic bending in the cantilever arms. Mathematically, ΔU can be derived from energy principles as the area under the load–displacement curve at a particular incremental crack length (Δa):

$$\Delta U = \int_0^{\hat{\delta}} P d\hat{\delta}\Big|_{\Delta a}, \tag{2}$$

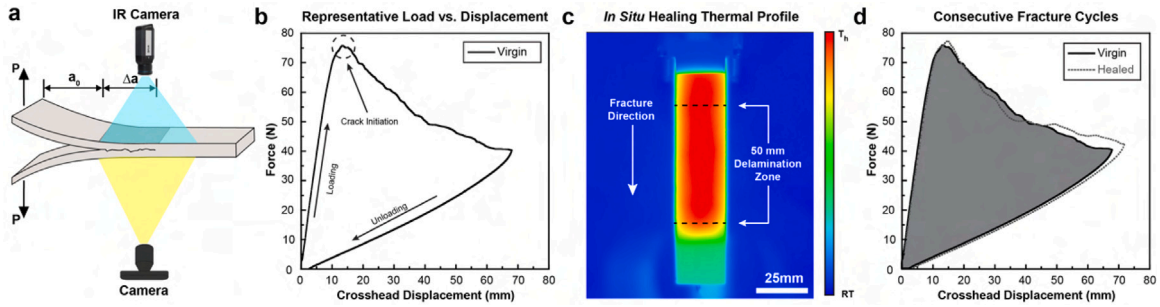

Fig. 2. Mode-I Fracture and *In Situ* Healing Evaluation. **(a)** Schematic of a double cantilever beam (DCB) test with underneath camera for crack tracking and overhead infrared (IR) camera for temperature monitoring. **(b)** Representative load versus displacement behavior for a virgin DCB specimen. **(c)** Top surface temperature distribution of a fractured DCB sample during a self-healing thermal remending cycle, as measured by an IR camera. **(d)** Overlaid virgin and healed load versus displacement curves for a DCB specimen, with the shaded area representing the change in internal work for the virgin sample (ΔU).

Table 2
Equivalent healing temperatures and equivalent viscosities for each EMAA variant considered in this study. Approximate electrical power requirements to achieve each healing temperature are provided in parentheses.

Polymer	Equivalent temperature (130 °C) Viscosity (Pa·s)	Equivalent Viscosity (1528 Pa·s) Temperature (°C)
Nucrel™ 2940	452 (12 W)	109 (9 W)
Nucrel™ 960	3458 (12 W)	146 (14 W)
Surlyn™ PC-2200	5808 (12 W)	166 (17 W)
Surlyn™ 1702	11953 (12 W)	170 (18 W)

where P represents the measured force at a prescribed crosshead displacement $\hat{\delta}$. (To avoid conflict in notation with $\tan(\delta)$, employed in the dynamic mechanical analysis discussed prior, we have used $\hat{\delta}$ to denote the displacement.) Healing efficiency is calculated as the ratio between healed and virgin critical strain energy release rates according to the established relation [22,23,49]:

$$\hat{\eta} := \frac{G_{IC}^{healed}}{G_{IC}^{virgin}} \times 100, \tag{3}$$

where $\hat{\eta}$ is the healing efficiency expressed in percentage, and G_{IC}^{virgin} and G_{IC}^{healed} are the virgin and healed critical strain energy release rates, respectively.

2.6. Chemical and topological characterization of fracture surfaces

2.6.1. Scanning electron microscopy (SEM)

Scanning electron micrographs were acquired using a SU3900 variable pressure scanning electron microscope (Hitachi, Ltd.) at a 10 kV accelerating voltage after sputtering the samples with gold/palladium to a target coating thickness of 10 nm.

2.6.2. Fourier transform infrared (FTIR) spectroscopy

Spectroscopy was performed on post-fractured DCB sections using an FTIR microscope (Hyperion 1000 microscope with a Tensor 27 spectrometer, Bruker, Inc.) in Attenuated Total Reflectance (ATR) mode with a 70 μm germanium crystal probe and 20x objective. 32 scans were collected at each sampling site from the 650 cm^{-1} to 4000 cm^{-1} wavenumber range.

3. Results

We examine the effects of EMAA chemistry, melt viscosity, and healing temperature on fracture recovery via thermal remending. Glass fiber-reinforced polymer (GFRP) composite DCB samples containing midplane interlayers (at 16% areal coverage ≈ 0.94 vol%) of the four selected EMAA variants are tested for one virgin fracture cycle and ten successive heal-fracture cycles at both equivalent healing temperature (130 °C) and equivalent melt viscosity (1528 Pa·s) conditions. We sought to assess the influence(s) of molten EMAA physical spreading and chemical reactivity (with the epoxy matrix) during healing. To eliminate potential contributions of matrix mobility on fracture recovery behavior, thermal remending temperatures are kept well below the T_g of the GFRP but above the melting temperature range (83 to 93 °C) of the EMAA variants (Appendix A.1); Fig. 3a shows that the T_g (i.e., the peak of $\tan(\delta)$) in the GFRP is approximately 195 °C. As Fig. 3b shows, melt viscosities of the EMAA variants differ at the chosen equivalent healing temperature (130 °C), and the required healing temperatures T_h differ for the equivalent viscosity condition (1528 Pa·s).

As shown in Figs. 4a and 4b, GFRP augmented with the non-neutralized Nucrel™ copolymers display similar virgin mode-I critical strain energy release rate (G_{IC}) values of ≈ 1100 J/m^2. The Na^+-neutralized Surlyn™ PC-2200 ionomer virgin G_{IC} is significantly lower (≈ 500 J/m^2) and the Zn^{2+}-neutralized Surlyn™ 1702 ionomer value slightly higher (≈ 1300 J/m^2). Regardless of the EMAA variant or healing condition, the G_{IC} of heal cycle 1 is lower than the virgin value since the discrete EMAA domains do not cover the entire fracture surface where non-coated regions (i.e., epoxy/fiber) are not repairable. Coinciding with greater observed fibrillation during fracture, tensile testing of each EMAA variant Appendix A.2 reveals that the copolymers display superior ductility to the ionomers.

Shown in Figs. 4a and 4c, healing at an *equivalent temperature* of 130 °C (differing viscosities), the restoration of G_{IC} relative to the virgin cycle correlates inversely with melt viscosity (η); Nucrel™ 2940 (lowest η, ≈ 452 Pa·s) exhibits the highest healing efficiency, and Surlyn™ 1702 (highest η, ≈ 11953 Pa·s) the lowest healing efficiency. Figs. 4b and 4d show that healing at *equivalent viscosity* (1528 Pa·s) produces a similar degree of recovery in the Nucrel™ copolymers despite significantly different healing temperatures (109 °C for 2940 vs. 146 °C for 960). Despite Nucrel™ 960 also having less methacrylic acid content (15 wt%) than Nucrel™ 2940 (19 wt%), we believe that their similar healing performance is due to the higher healing temperature of 960 increasing the rate of aforementioned condensation reactions with the epoxy matrix [39,42], whereby similar melt-spreading to 2940 can be achieved via pressure delivery. The Surlyn™ ionomers, despite having similar healing temperatures for the equivalent viscosity condition (within 4 °C), behave quite differently. PC-2200 exhibits the lowest virgin and healed G_{IC}, which remains fairly consistent over multiple healing cycles. Conversely, 1702 displays progressive degradation in

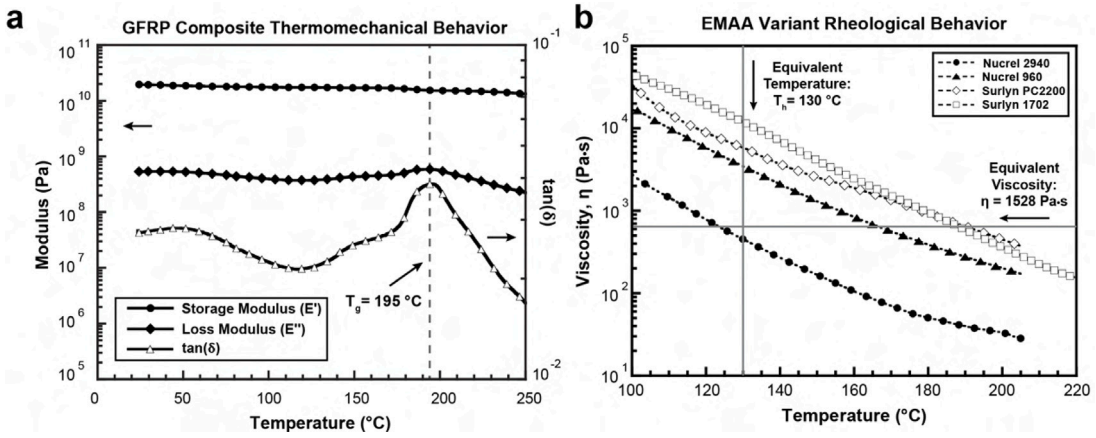

Fig. 3. *In Situ* Self-healing Conditions. **(a)** Thermomechanical behavior of a plain GFRP composite (assessed via DMA), with the $T_g \approx 195\,°C$ indicated by dashed line. **(b)** Melt viscosity comparison of copolymers (Nucrel™) and ionomers (Surlyn™) with equivalent healing temperature (130 °C) and viscosity (1528 Pa·s) conditions indicated by vertical and horizontal lines, respectively.

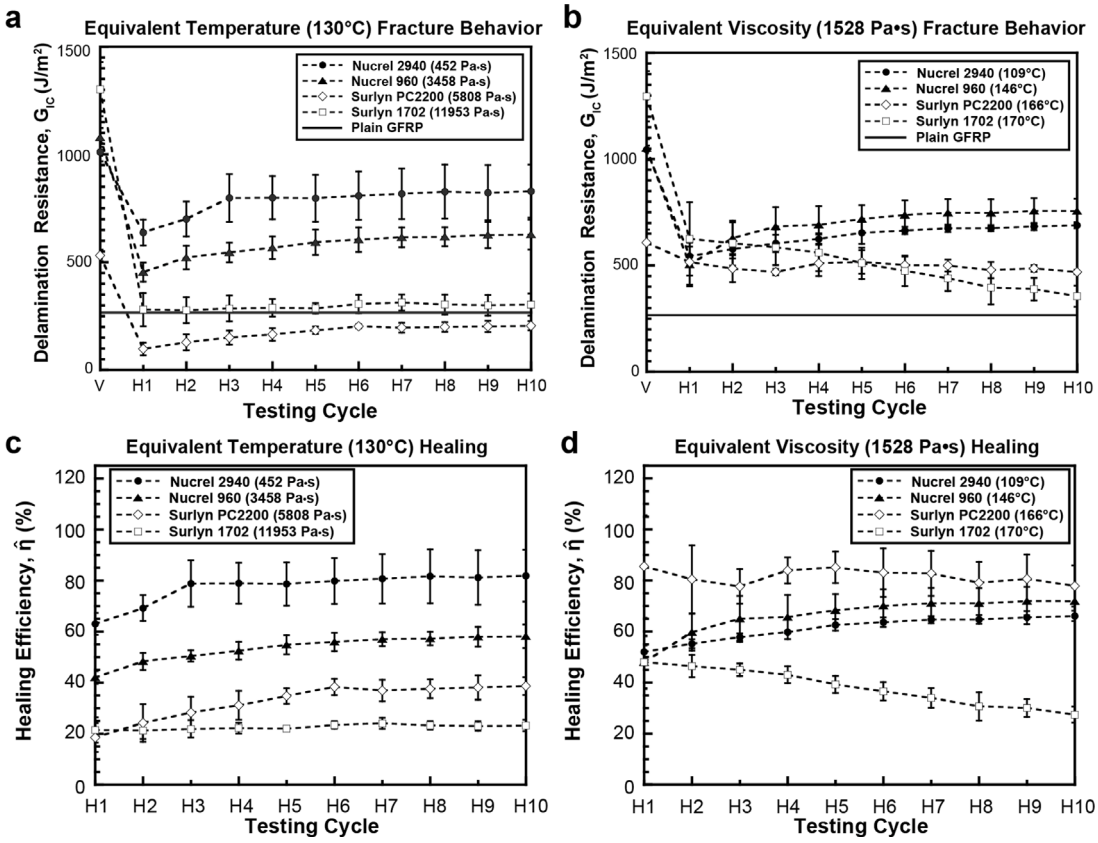

Fig. 4. Fracture/Healing Comparison. Delamination resistance evolution versus test cycle for FRP healed at: **(a)** Equivalent temperature (130 °C) conditions and **(b)** Equivalent viscosity (1528 Pa·s) conditions. Calculated healing efficiency for each EMAA variant tested at: **(c)** Equivalent temperature (130 °C) and **(d)** Equivalent viscosity (1528 Pa·s) conditions. Error bars represent one standard deviation from the mean ($n = 3$).

healed G_{IC} values with test cycle accumulation. Figs. 4c and 4d summarize healing efficiency (the ratio of healed to virgin G_{IC} restoration) for each EMAA variant at the equivalent healing temperature (130 °C) and equivalent melt viscosity (1528 Pa·s), respectively. At the equivalent healing temperature, only the Nucrel™ 2940 has low enough melt viscosity to spread significantly during remending, resulting in greater areal coverage across the fracture plane and thereby increasing healing efficiency ($\hat{\eta}$), especially in early cycles. The 2940 eventually reaches $\hat{\eta} \approx 80\%$ versus 50% for the 960 and 20%–30% for the two Surlyn™ ionomers, which display little to no spreading. Differences in spreading behavior are evidenced by the initial increase and eventual plateau in healed G_{IC} [49], which is less pronounced for the 960 copolymer and not present for the EMAA ionomers (1702, PC-2200). As Fig. 4d shows, the copolymers exhibit similar healing efficiency ($\hat{\eta} \approx 70\%$) at equivalent melt viscosity (1528 Pa·s). Interestingly, the Surlyn™ PC-2200 exhibits higher and more consistent healing efficiency ($\hat{\eta} \approx 80\%$), though the healed fracture resistance ($G_{IC} \approx 400\ J/m^2$) is significantly lower than either of the two copolymers ($\approx 700\ J/m^2$). Surlyn™ 1702 exhibits the lowest healed G_{IC}, continually decreasing from an initial value of $\approx 700\ J/m^2$ to $\approx 400\ J/m^2$. The contrasting healing efficiencies of the two ionomers with different neutralization groups cannot be solely attributed to melt-flow behavior, as neither variant demonstrated

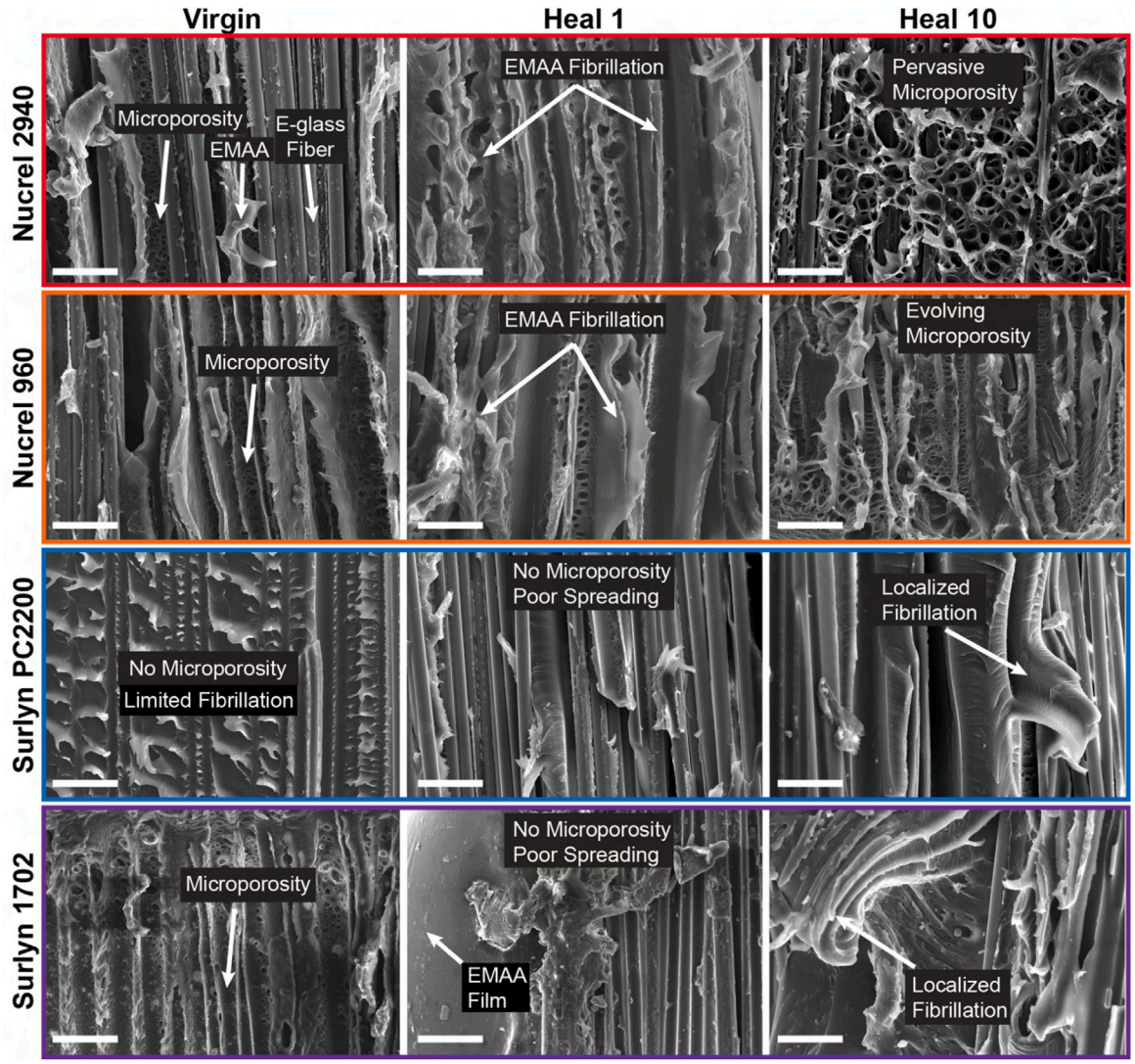

Fig. 5. Equivalent Healing Temperature (130 °C) Fracture Topology. Scanning electron micrographs showing evolution of virgin and healed fracture topology for each EMAA variant after testing at the equivalent temperature condition. Scale bars = 25 μm.

markedly different spreading, thus driving further investigation into potential topological and chemical contributions. Additionally, to assess whether healing can occur in the absence of either EMAA or thermal stimulus, two types of control samples are evaluated: (i) *in situ* heated, but not containing EMAA, (ii) non-heated and containing each respective EMAA variant printed at 16% areal coverage. None of the control samples exhibit any measurable fracture recovery (Appendix A.4).

To better understand mechanistic differences underlying healing performance in the four EMAA variants, scanning electron microscopy (SEM) is conducted on fracture surfaces of DCB specimens after the virgin, heal 1, and heal 10 cycles at each thermal remending condition. Specifically, differences in fracture topology, EMAA spreading, and microporosity–created by evolution of water vapor during EMAA-OH group condensation reactions [42]–are examined. Differences in healing mechanisms between the four variants at each healing condition are then assessed. Fig. 5 reveals distinctions in fracture topology of the four EMAA variants following the virgin test cycle, heal 1, and heal 10 conducted at equivalent healing temperatures (130 °C). The copolymers show a greater degree of melt-spreading, fibrillation, and microporous network evolution compared to the ionomers. Since the copolymers are less viscous than the ionomers at this condition (2940: 452 Pa·s, 960: 3458 Pa·s, PC-2200: 5808 Pa·s, 1702: 11953 Pa·s), the stark difference in microporosity between the two groups indicates that the ionomers do not benefit from a pressure-delivery mechanism (i.e., EMAA-OH group reactivity) at this condition and thus display poor healing. Both copolymers exhibit significant microporous network formation and growth (2940 more so than 960), whereas the PC-2200 shows no microporous network development and the 1702 exhibits microporosity induced by initial composite cure, but not sustained during healing. This limited microporosity in the ionomers, despite similar non-neutralized methacrylic acid concentrations (≈ 15 wt%) to the copolymers, suggests reduced physical mobility is responsible for mitigation of EMAA-epoxy reactions. The reduced mobility is likely a combination of high polymer melt viscosities at 130 °C and/or physical crosslinking caused by the metallic ions introduced through neutralization. Furthermore, the lack of fibrillation in the ionomers even after repeated healing cycles corroborates with lower ductility observed during tension testing (Fig. A.2), resulting in less energy dissipation during mode-I fracture propagation compared with the copolymers. The 2940 shows superior fracture recovery over the 960 at the 130 °C healing temperature ($\hat{\eta} \approx 80\%$ versus 50%, respectively), likely due to lower viscosity and increased reactivity with the epoxy matrix owing to greater methacrylic acid content (19 wt% vs. 15 wt%).

Fig. 6 reveals fracture topology differences for each EMAA variant after the virgin test and heal cycles 1 and 10 conducted at equivalent melt viscosity (1528 Pa·s). Contrasting with the equivalent healing temperature at 130 °C, Nucrel™ 2940 displays less microporous network

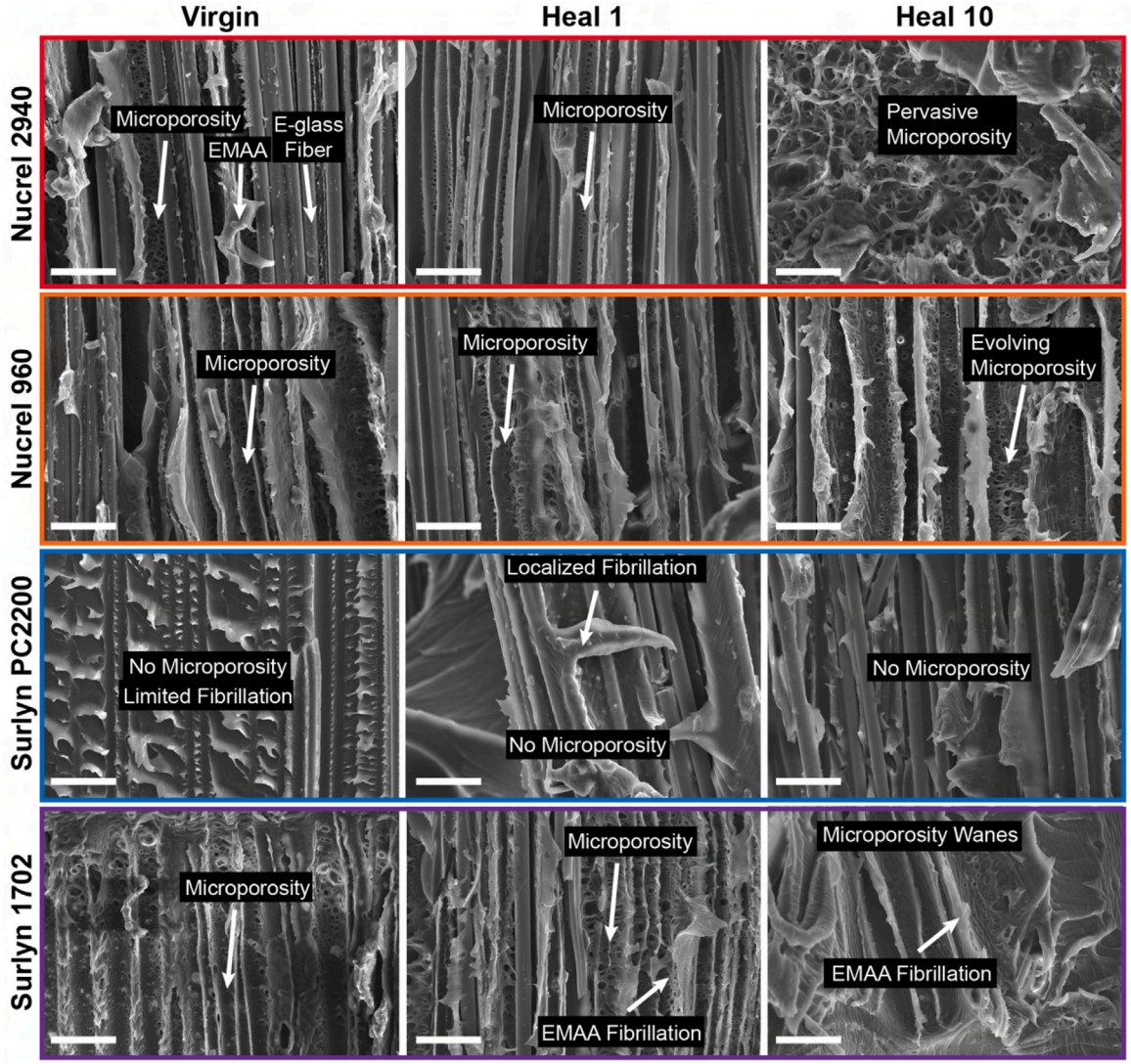

Fig. 6. Equivalent Healing Viscosity (1528 Pa·s) Fracture Topology. Scanning electron micrographs showing evolution of virgin and healed fracture topology for each EMAA variant after testing at the equivalent viscosity condition. Scale bars = 25 μm.

growth due to the lower healing temperature (109 °C) likely slowing EMAA-epoxy reaction kinetics. Conversely, Nucrel™ 960 displays a greater degree of microporosity at heal 1 and a more diffuse microporous network at heal 10 due to a higher healing temperature of 146 °C. These healing temperature differences correlate with a reduced healing efficiency for 2940 ($\hat{\eta} \approx 80\%$ to $\hat{\eta} \approx 70\%$) and increased healing efficiency for 960 ($\hat{\eta} \approx 40\%$ to $\hat{\eta} \approx 70\%$). Thus, increased healing efficiency observed in the 960 is attributed to the higher healing temperature, reduced melt viscosity, and increased rates of EMAA-hydroxyl condensation reactions. Despite a significantly higher healing temperature (166 °C) compared to the reference of 130 °C, Surlyn™ PC-2200 exhibits no microporous network formation and poor ductility, even at a much lower melt viscosity (1528 Pa·s vs. 5808 Pa·s). While healing efficiency is greater at 166 °C ($\hat{\eta} \approx 80\%$) than at 130 °C ($\hat{\eta} \approx 30\%$), the restored G_{IC} values are less than half that of either copolymer and any improvements are likely due to molten spreading caused by mechanical cycling. A comparison of the virgin fracture behavior between ionomers shows the 1702 has a higher G_{IC} than that of the PC-2200 (≈ 1300 vs. ≈ 500 J/m^2), where neither variant showed significant ductility nor fibrillation during virgin fracture. Interestingly, Surlyn™ 1702 displays a topological transition from a non-ductile fracture surface to ductile fibrillation via melt viscosity reduction at the higher healing temperature ($\approx$ 1,500 Pa·s at 170 °C vs. $\approx$ 12,000 Pa·s at 130 °C). More significant is the observed increase in microporosity for Surlyn™ 1702 from the virgin cycle to heal 1, but a collapse thereafter, indicating that EMAA-hydroxyl reactions were initially produced by healing at 170 °C, but eventually cease [49]. This coincides with a progressive decrease in healing efficiency from heal cycle 1 ($\hat{\eta} \approx 50\%$) to heal 10 ($\hat{\eta} \approx 25\%$).

Based on aggregation of SEM images and fracture data, the copolymers are shown to be superior healants compared to the ionomers. The copolymers possess greater chemical reactivity with the epoxy matrix and lower melt viscosities, which facilitate spreading during pressure delivery. Furthermore, healed G_{IC} values are higher in the copolymers due to pervasive microporosity inducing crack tortuosity, thus increasing the resistance to crack propagation. Comparing the ionomers, Surlyn™ PC-2200 exhibits negligible microporous network evolution/reactivity with the underlying matrix and steady healing performance at either condition tested, though lowering melt viscosity improves healing efficiency at the relatively modest G_{IC} values noted. Surlyn™ 1702, on the other hand, displays negligible healing and reactivity with the matrix at 130 °C, but significant initial healing and reactivity at 170 °C; though both progressivly decrease from heal 1 to heal 10. These differences in Surlyn™ PC-2200 and 1702 reactivity can be attributed to different neutralization in each ionomer. Na^+-neutralization in PC-2200 produces much larger (and less mobile) ionic

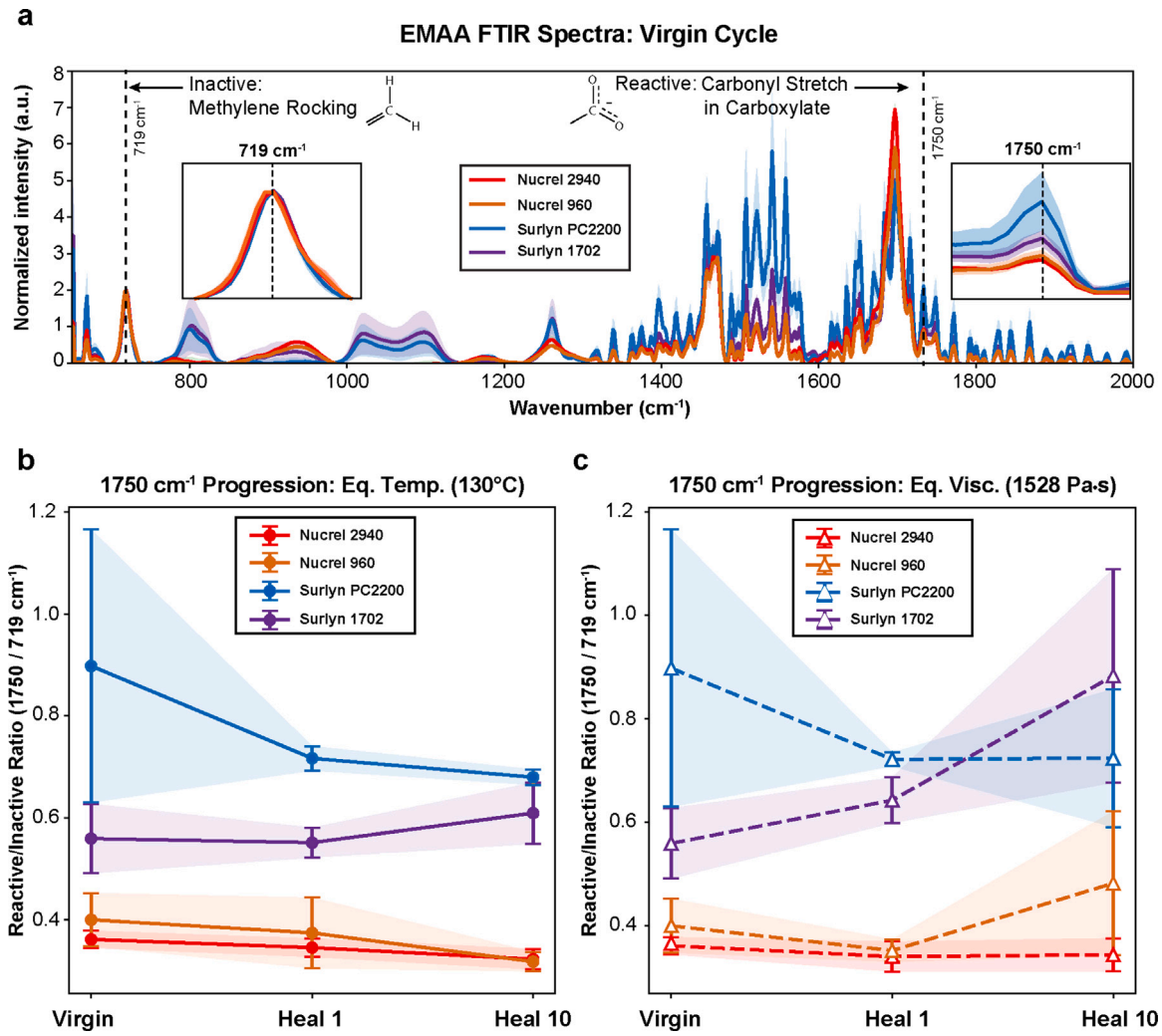

Fig. 7. FTIR-ATR Spectroscopy of EMAA. **(a)** Overlaid FTIR spectra of all EMAA variants following the virgin fracture cycle, with inactive (719 cm^{-1}) and reactive (1750 cm^{-1}) peaks of interest labeled. Reactive-to-inactive spectral ratio progression of each EMAA variant for the: **(b)** Equivalent temperature and **(c)** Equivalent viscosity healing conditions. Shading represents one standard deviation from the mean (n = 5).

aggregates (i.e., physical crosslinks) relative to Zn^{2+}-neutralization in 1702 [51]. However, SEM studies alone are insufficient to determine why the 1702 ionomer exhibits early reactivity with the epoxy matrix at the higher healing temperature.

Thus, FTIR-ATR spectroscopy is leveraged to interrogate the signature of the reactive carboxylate group carbonyl stretching peak at 1750 cm^{-1} relative to an inactive methylene rocking peak at 719 cm^{-1} [49]. Fig. 7a shows the spectral signatures for each EMAA variant, measured on fractured DCB surfaces following the virgin cycle, with these peaks of interest labeled. The ratio of carboxyl to methylene peak absorbances is not expected to change with healing cycle count as carboxyl groups are neither consumed nor produced during healing reactions. However, this assumption does not hold for Surlyn™ 1702. As shown in Figs. 7b and 7c, an increasing trend of carboxyl spectral intensity is observed through successive cycles, especially for the equivalent viscosity healing conducted at 170 °C. The increase in reactive to inactive peak ratios after healing can explained by the movement of bivalent Zn^{2+} salts (and associated physical crosslinks) to the epoxy-EMAA interface at elevated temperatures, which suppress interfacial EMAA-epoxy reactions while effectively increasing the free carboxyl concentration away from these interfaces. This migration is driven by the high affinity of Zn^{2+} for amines present in the epoxy matrix due to atomic coordination by nitrogen atoms [68,69]. Such behavior has been previously leveraged to improve surface adhesion of polyethylene to epoxy using zinc [70]. While more mobile physical crosslinking in ionomers can enable some degree of reaction with epoxy, migration of metallic ion species (such as Zn^{2+}) to the matrix precludes interfacial reaction progression and degrades healing performance in successive cycles.

In summary, non-neutralized EMAA copolymers are superior to ionomers for healing mode-I fracture damage in GFRP composites. In addition to low melt viscosity enabling infiltration and fusion of larger and more diffuse fracture regions during thermal remending, superior copolymer ductile fracture behavior is further aided by greater reactivity with the epoxy matrix. In other words, pressure delivery of molten healant increases fracture surface coverage whereby microporous network formation and growth enhances crack tortuosity (i.e., crack growth resistance).

4. Closure

This article examines 3D-printed non-neutralized (copolymer) and neutralized (ionomer) EMAA thermoplastics as self-healing interlayers in GFRP composites by leveraging an *in situ* thermal remending strategy. Notably, neutralized EMAA ionomers that have proven effective as self-healing films in heat-producing ballistic applications [52] are inferior to their non-neutralized counterparts for healing mode-I fracture via thermal remending in laminated composites. While increased

methacrylic acid concentrations and reactivity (i.e., no neutralization) correlate with superior healed G_{IC} and greater microporous evidence of EMAA-hydroxyl reactions, low melt viscosity also drives fracture recovery as pressure delivery of EMAA enables infiltration and rebonding of crack surfaces. Additionally, the type of metallic ion selected for neutralization influences healing behavior. Na^+ ions form relatively immobile physical crosslinks which inhibit reactions with the epoxy matrix, whereas Zn^{2+} produces smaller ionic aggregates (i.e., mobile crosslinks) which progressively impede these reactions, as Zn^{2+} has a propensity to migrate to the epoxy-EMAA interface.

Thus, this study provides newfound insight into EMAA physical/chemical alterations that affect self-healing of interlaminar delamination. Such contributions promise to further the potential for service lifetime extension of composite structures while lowering their associated economic and environmental costs. Future work can leverage these findings to tailor EMAA and composite constituent chemical couplings to maximize virgin fracture resistance and subsequent self-healing capacity under varying thermal remending conditions.

CRediT authorship contribution statement

Alexander D. Snyder: Writing – review & editing, Writing – original draft, Visualization, Investigation, Formal analysis. **Jack S. Turicek:** Writing – review & editing, Writing – original draft, Visualization, Investigation, Formal analysis. **Charles E. Diesendruck:** Writing – review & editing, Writing – original draft, Formal analysis. **Russell J. Varley:** Writing – review & editing, Writing – original draft, Formal analysis. **Jason F. Patrick:** Writing – review & editing, Writing – original draft, Supervision, Project administration, Methodology, Funding acquisition, Data curation, Conceptualization.

Declaration of competing interest

The authors declare the following financial interests/personal relationships which may be considered as potential competing interests: Jason F. Patrick reports financial support was provided by Strategic Environmental Research and Development Program. Jason F. Patrick and Alexander D. Snyder have a patent issued to NC State University. If there are other authors, they declare that they have no known competing financial interests or personal relationships that could have appeared to influence the work reported in this paper.

Data availability

Data will be made available on request.

Acknowledgments

The authors acknowledge the financial support from the Strategic Environmental Research and Development Program, United States (SERDP) through grant No. W912HQ21C0044 awarded to J.F.P. The work was performed in part at the Analytical Instrumentation Facility (AIF) at North Carolina State University, which is supported by the State of North Carolina and the National Science Foundation (grant ECCS-2025064). The AIF is a member of the North Carolina Research Triangle Nanotechnology Network (RTNN), a site in the National Nanotechnology Coordinated Infrastructure (NNCI). The authors extend their gratitude to Dr. Masihullah J. Khan of the Institute for Frontier Materials at Deakin University for assistance with EMAA filament extrusion and rheological characterization, and Dr. Carrie Donley at the Chapel Hill Analytical and Nanofabrication Laboratory (CHANL) for assistance with FTIR spectroscopy. This material is based upon work supported by the National Science Foundation Graduate Research Fellowship Program under Grant No. DGE-2137100. Any opinions, findings, and conclusions or recommendations expressed in this material are those of the author(s) and do not necessarily reflect the views of the National Science Foundation.

Appendix A

A.1. Differential scanning calorimetry (DSC) of EMAA variants

Differential scanning calorimetry (DSC) was performed on samples excised from extruded EMAA filament and contained in hermetically sealed aluminum pans with a heat-flux DSC (TA Instruments, Inc.). Samples were cooled to 0 °C and held for 5 min before being heated to 300 °C at 10 °C/min, and then cooled to 25 °C at a rate of 10 °C/min to complete a full heat-cool cycle. As displayed in Fig. A.1, all EMAA variants show consistent melt-recrystallization behavior through consecutive cycles and have melting temperatures between 83 °C and 93 °C (Table A.1).

A.2. Tension testing of EMAA variants

For each of the four EMAA polymers, injection molded dogbone samples (Type IV geometry, ≈ 1.2 mm thick) were produced according to the process parameters detailed in Table A.2. To ensure that the properties of the samples were approximately representative of 3D-printed domains, the parameter sets were chosen to minimize residual stress, limit shrinkage, and avoid molding pressures linked to high degrees of crystallinity.

Tensile testing was conducted in accordance with ASTM D638. Displacement-controlled loading was applied to each sample at 20 mm/min using a 10 kN electromechanical load frame (MTS, Inc.) equipped with a 500 N load cell, while concurrent images for Digital Image Correlation (DIC) were acquired on the front and back gauge face of each sample using 12.3 MP machine vision cameras (GS3-U3-123S6M-C, Teledyne FLIR, Inc.). Full-field strains were calculated on the observed faces using Vic-2D software (Correlated Solutions, Inc.), as shown in Fig. A.2a. Representative load–displacement behavior for each polymer is displayed in Fig. A.2b, with the ionomers noticeably stiffer than the copolymers. Though the plastic deformation sustained in each polymer (failure strains exceed 100%) precludes DIC image correlation beyond the initial portion of testing (Fig. A.2c), calculation of primary tensile properties was still possible as provided in Table A.3.

A.3. Cross-sectional geometry of EMAA-modified composites

Representative cross-sections of self-healing composites at various loading stages are shown in Fig. A.3, including: (a) pristine glass-fiber composite containing 3D-printed EMAA (Nucrel™ 2940), (b) fractured double-cantilever beam with midplane delamination, (c) self-healed composite after *in situ* thermal remending with EMAA rebonding crack.

A.4. Non-healing controls

GFRP DCB control specimens containing resistive heaters, but no EMAA, with a stacking sequence of $[0/90]_2$-heater-$[0/90]_3$-heater-$[0/90]_2$ were investigated to determine whether healing occurs without EMAA interlayers. In addition, control specimens containing a 16% serpentine midlayer pattern of each EMAA variant and a stacking sequence of $[0/90]_2$-heater-[0/90/0]-EMAA-[90/0/90]-heater-$[0/90]_2$ were investigated to assess whether remending of EMAA occurs without applied heat. Three specimens of each were fabricated and evaluated using the same test procedure described for self-healing specimens in the main text. Fig. A.4a shows a representative load–displacement curve for the virgin and one subsequent test cycle for a non-EMAA control after *in situ* heating at 170 °C (the highest healing temperature in this work) and Fig. A.4b–e show representative load–displacement curves for the virgin and one subsequent test cycle after a 45-minute dwell at RT for the non-heated controls containing EMAA. In either case, there was a negligible recovery of virgin fracture resistance, evidenced by the loading/unloading curves following the same path and having nearly equivalent compliance (i.e., identical crack length) as the unloading curve from the virgin cycle.

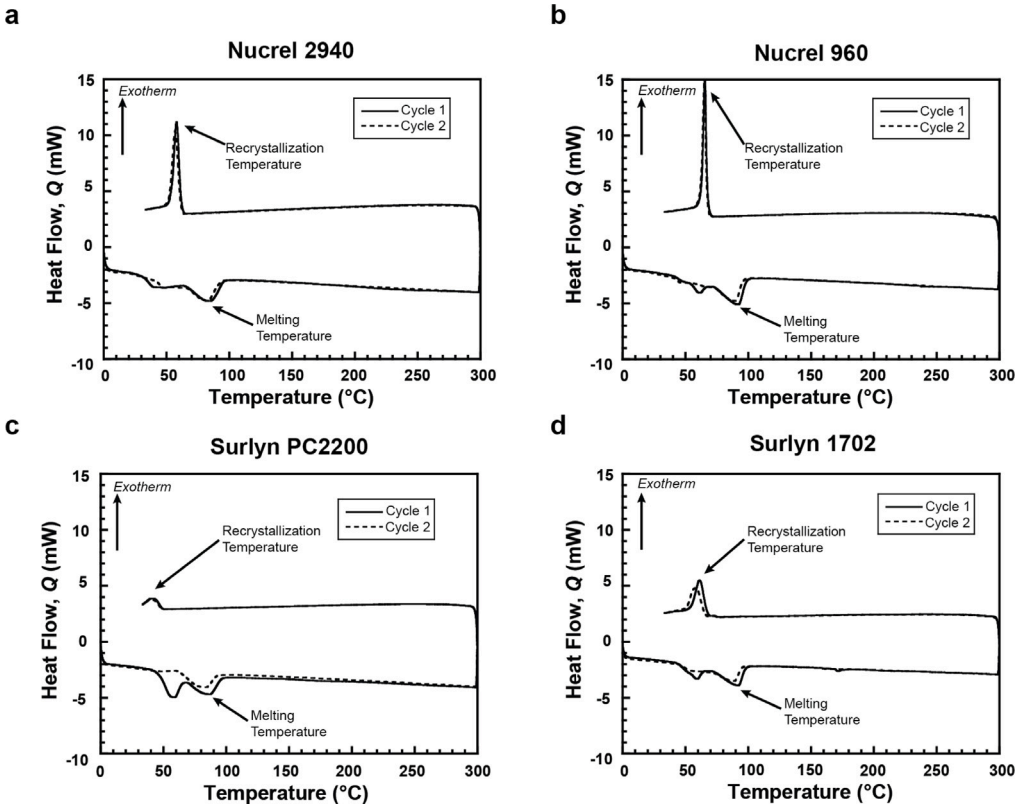

Fig. A.1. DSC of EMAA Variants. Repeated heat-cool phase change behavior for **(a)** Nucrel™ 2940, **(b)** Nucrel™ 960, **(c)** Surlyn™ PC-2200, and **(d)** Surlyn™ 1702.

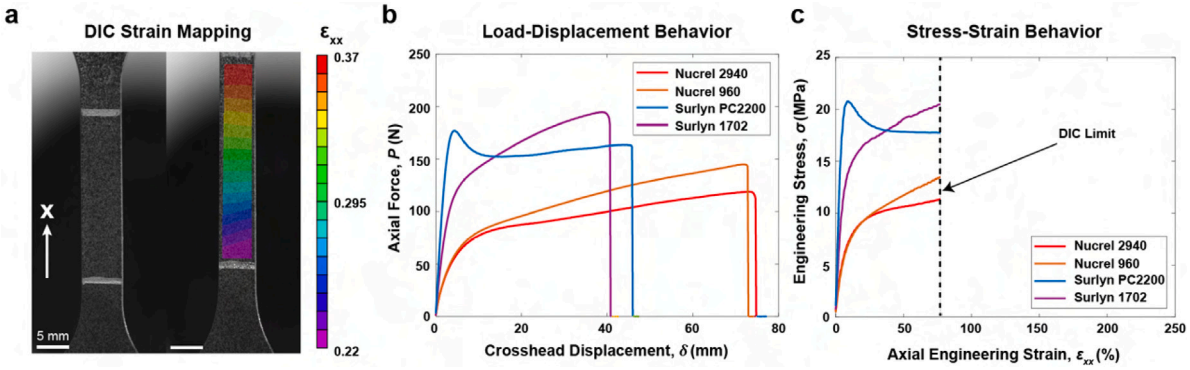

Fig. A.2. Tensile Behavior of EMAA Variants. **(a)** DIC speckle pattern and overlaid axial strain contours on a ≈ 25 mm long gauge section. **(b)** Representative load versus crosshead displacement behavior for each polymer. **(c)** Calculated stress–strain values for each polymer, with the point of loss in digital image correlation (DIC) labeled.

Table A.1
EMAA variant melting and recrystallization temperatures.

Polymer	DSC cycle	Melting temperature (°C)	Recrystallization temperature (°C)
Nucrel™ 2940	1	84.8	58.1
	2	83.2	57.0
Nucrel™ 960	1	93.2	65.5
	2	90.5	65.0
Surlyn™ PC-2200	1	87.7	40.8
	2	83.8	42.2
Surlyn™ 1702	1	92.8	61.5
	2	89.3	58.4

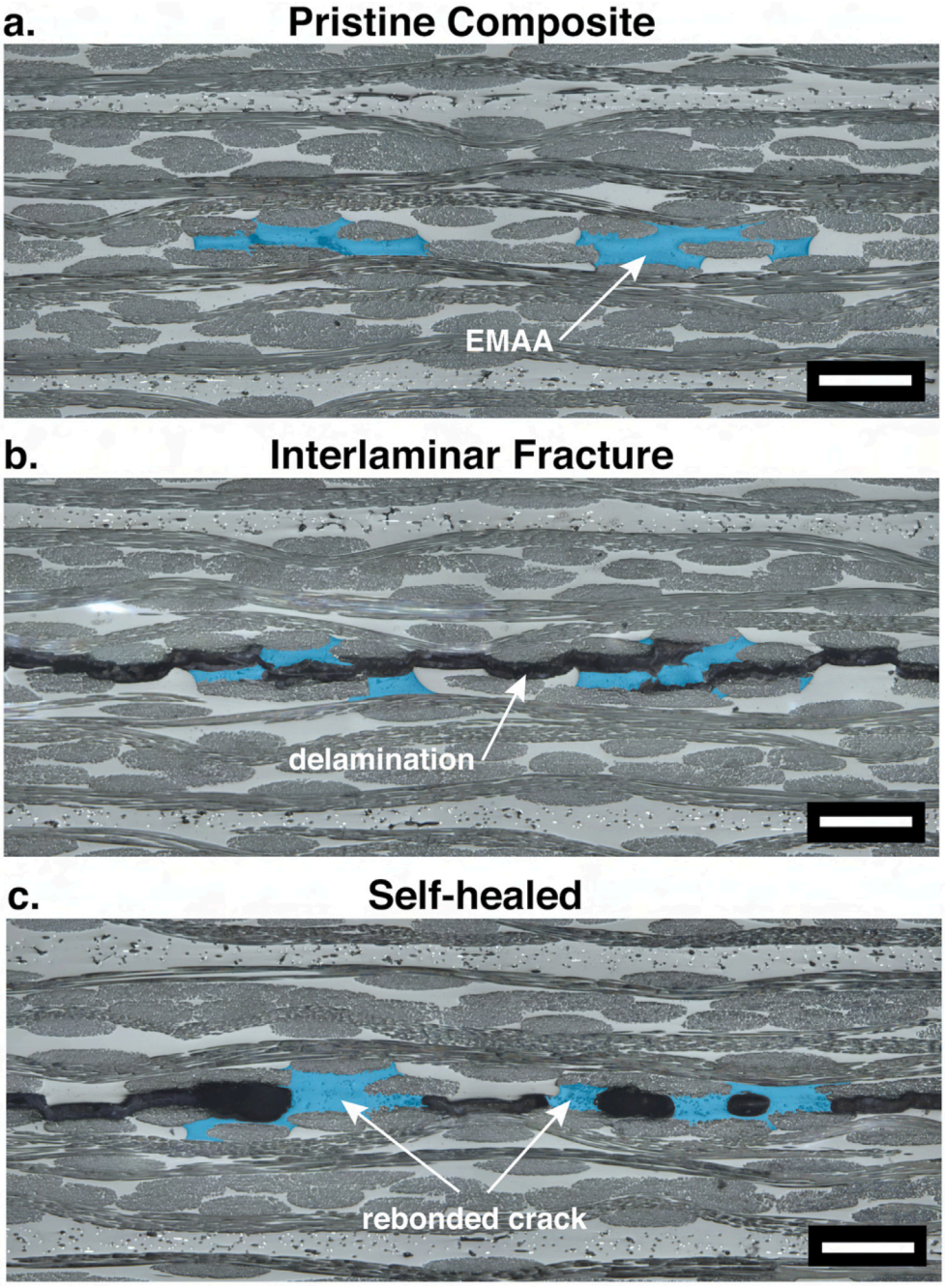

Fig. A.3. GFRP Composite Cross-sections. **(a)** Pristine laminate with 3D-printed EMAA domains post melt consolidation. **(b)** Fractured composite with mid-layer delamination. **(c)** Self-healed laminate with rebonded crack via *in situ* thermal remending of EMAA. Scale bars = 500 μm.

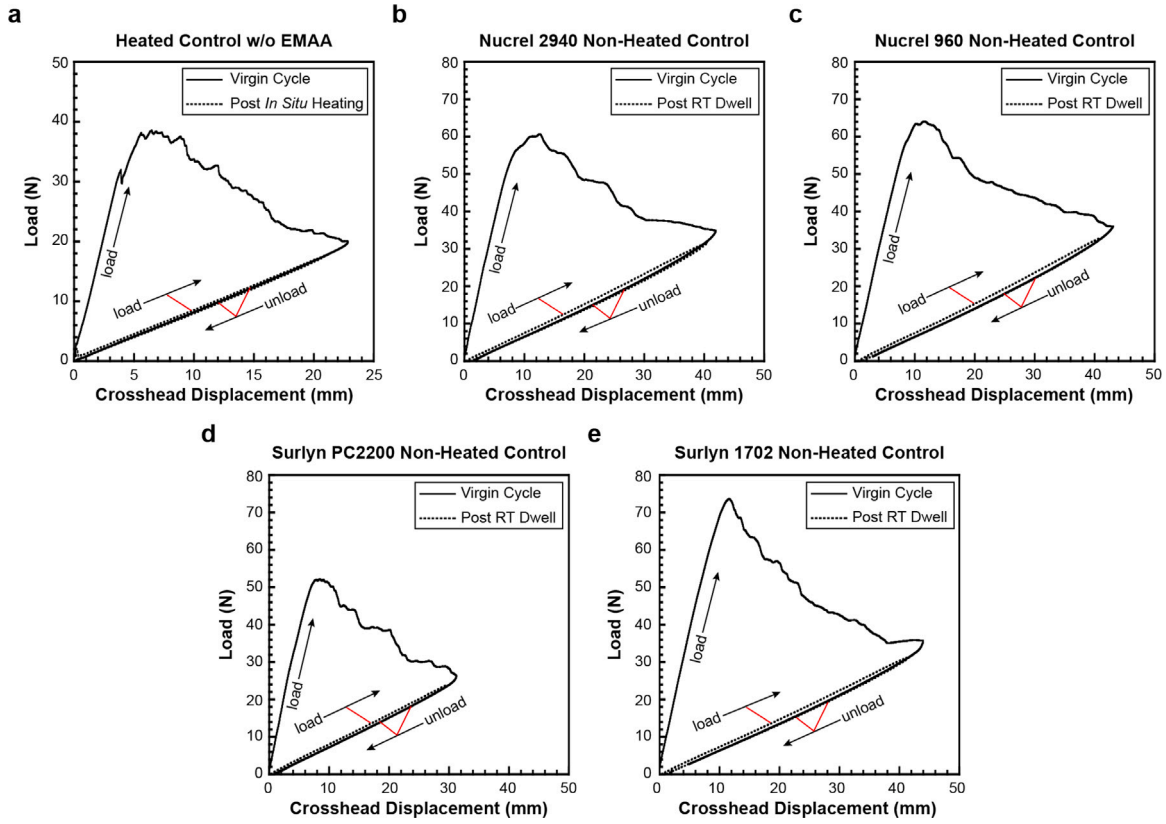

Fig. A.4. Mode-I Fracture of Non-healing Controls. **(a)** Representative DCB load–displacement behavior for a sample with resistive heaters, but no EMAA—after the virgin and one subsequent test cycle following *in situ* heating (170 °C) / cooling. Samples with a 16% midlayer EMAA pattern of: **(b)** Nucrel™ 2940 **(c)** Nucrel™ 960 **(d)** Surlyn™ PC-2200 **(e)** Surlyn™ 1702—after the virgin and one subsequent test cycle following a room temperature (RT) dwell for 45 min (i.e., the same length of time as a typical heating/cooling cycle).

Table A.2
EMAA injection molding process parameters.

Polymer	Residence time (min)	Melt temperature (°C)	Injection pressure (psi)	Injection time (s)	Mold temperature (°C)	Packing pressure (psi)	Packing time (s)	Cycle time (s)
Nucrel™ 2940	13.2	131	4300	0.34	24	4000	3	38
Nucrel™ 960	13.5	178	5100	0.34	24	4300	3	43
Surlyn™ PC-2200	13.6	199	5200	0.34	26	4700	3	57
Surlyn™ 1702	13.3	195	6100	0.34	26	5900	3	49

Table A.3
EMAA variant tensile properties.

Polymer	Elastic modulus (MPa)	Poisson's Ratio	Ultimate strength (MPa)	Toughness (J/m^2)
Nucrel™ 2940	96.4 ± 14.8	0.47 ± 0.02	14.3 ± 0.1	7.0 ± 0.4
Nucrel™ 960	100.0 ± 10.6	0.47 ± 0.01	17.8 ± 0.5	8.0 ± 0.4
Surlyn™ PC-2200	395.5 ± 12.1	0.48 ± 0.01	19.0 ± 0.6	7.1 ± 0.8
Surlyn™ 1702	206.3 ± 16.6	0.46 ± 0.02	22.5 ± 0.9	5.9 ± 0.6

References

[1] Cantwell WJ, Morton J. The significance of damage and defects and their detection in composite materials: A review. J Strain Anal Eng Des 1992;27(1):29–42.
[2] Wisnom MR. The role of delamination in failure of fibre-reinforced composites. Phil Trans R Soc A 2012;370(1965):1850–70.
[3] Wang B, Zhong S, Lee T-L, Fancey KS, Mi J. Non-destructive testing and evaluation of composite materials/structures: A state-of-the-art review. Adv Mech Eng 2020;12:1–28.
[4] Katnam KB, Da Silva LFM, Young TM. Bonded repair of composite aircraft structures: A review of scientific challenges and opportunities. Prog Aerosp Sci 2013;61:26–42.
[5] Heslehurst RB. Engineered repairs of composite structures. first ed.. Boca Raton: CRC Press / Taylor & Francis; 2019.
[6] Richardson MOW, Wisheart MJ. Review of low-velocity impact properties of composite materials. Composites A 1996;27(12):1123–31.
[7] Hart KR, Chia PX, Sheridan LE, Wetzel ED, Sottos NR, White SR. Comparison of compression-after-impact and flexure-after-impact protocols for 2D and 3D woven fiber-reinforced composites. Composites A 2017;101:471–9.
[8] Mouritz AP, Cox BN. A mechanistic approach to the properties of stitched laminates. Composites A 2000;31(1):1–27.
[9] Brandt J, Drechsler K, Arendts F-J. Mechanical performance of composites based on various three-dimensional woven-fibre preforms. Compos Sci Technol 1996;56(3):381–6.
[10] Mouritz A. Review of z-pinned composite laminates. Composites A 2007;38(12):2383–97.
[11] Mouritz AP, Cox BN. A mechanistic interpretation of the comparative in-plane mechanical properties of 3D woven, stitched and pinned composites. Composites A 2010;41(6):709–28.
[12] Andrew JJ, Srinivasan SM, Arockiarajan A, Dhakal HN. Parameters influencing the impact response of fiber-reinforced polymer matrix composite materials: A critical review. Compos Struct 2019;224:111007.
[13] Islam F, Caldwell R, Phillips AW, John NAS, Prusty BG. A review of relevant impact behaviour for improved durability of marine composite propellers. Composites 2022;8:100251.
[14] Post W, Susa A, Blaauw R, Molenveld K, Knoop RJI. A review on the potential and limitations of recyclable thermosets for structural applications. Polym Rev 2020;60(2):359–88.
[15] Patrick JF, Robb MJ, Sottos NR, Moore JS, White SR. Polymers with autonomous life-cycle control. Nature 2016;540(7633):363–70.
[16] White SR, Sottos NR, Geubelle PH, Moore JS, Kessler MR, Sriram SR, et al. Autonomic healing of polymer composites. Nature 2001;409(6822):794–7.
[17] Brown EN, White SR, Sottos NR. Microcapsule induced toughening in a self-healing polymer composite. J Mater Sci 2004;39(5):1703–10.
[18] Blaiszik BJ, Kramer SLB, Olugebefola SC, Moore JS, Sottos NR, White SR. Self-healing polymers and composites. Annu Rev Mater Res 2010;40(1):179–211.
[19] Kessler MR, Sottos NR, White SR. Self-healing structural composite materials. Composites A 2003;34(8):743–53.
[20] Patel AJ, Sottos NR, Wetzel ED, White SR. Autonomic healing of low-velocity impact damage in fiber-reinforced composites. Composites A 2010;41(3):360–8.
[21] Moll JL, Jin H, Mangun CL, White SR, Sottos NR. Self-sealing of mechanical damage in a fully cured structural composite. Compos Sci Technol 2013;79:15–20.
[22] Patrick JF, Hart KR, Krull BP, Diesendruck CE, Moore JS, White SR, et al. Continuous self-healing life cycle in vascularized structural composites. Adv Mater 2014;26(25):4302–8.
[23] Hart KR, Lankford SM, Freund IA, Patrick JF, Krull BP, Wetzel ED, et al. Repeated healing of delamination damage in vascular composites by pressurized delivery of reactive agents. Compos Sci Technol 2017;151:1–9.
[24] Patrick JF, Krull BP, Garg M, Mangun CL, Moore JS, Sottos NR, et al. Robust sacrificial polymer templates for 3D interconnected microvasculature in fiber-reinforced composites. Composites A 2017;100:361–70.
[25] Qamar IPS, Sottos NR, Trask RS. Grand challenges in the design and manufacture of vascular self-healing. Multifunct Mater 2020;3(1):013001.
[26] Wang S, Urban MW. Self-healing polymers. Nat Rev Mater 2020;5(8):562–83.
[27] Ikura R, Park J, Osaki M, Yamaguchi H, Harada A, Takashima Y. Design of self-healing and self-restoring materials utilizing reversible and movable crosslinks. NPG Asia Mater 2022;14:1–17.
[28] Diesendruck CE, Sottos NR, Moore JS, White SR. Biomimetic self-healing. Angew Chem Int Ed 2015;54(36):10428–47.
[29] Imato K, Nishihara M, Kanehara T, Amamoto Y, Takahara A, Otsuka H. Self-healing of chemical gels cross-linked by diarylbibenzofuranone-based trigger-free dynamic covalent bonds at room temperature. Angew Chem Int Ed 2012;51(5):1138–42.
[30] Chen X, Dam MA, Ono K, Mal A, Shen H, Nutt SR, et al. A thermally re-mendable cross-linked polymeric material. Science 2002;295(5560):1698–702.
[31] Post W, Cohades A, Michaud V, van der Zwaag S, Garcia SJ. Healing of a glass fibre reinforced composite with a disulphide containing organic-inorganic epoxy matrix. Compos Sci Technol 2017;152:85–93.
[32] Cohades A, Branfoot C, Rae S, Bond I, Michaud V. Self-healing materials: Progress in self-healing fiber-reinforced polymer composites. Adv Mater Interfaces 2018;5(17):1870084.
[33] Sharma H, Rana S, Singh P, Hayashi M, Binder WH, Rossegger E, et al. Self-healable fiber-reinforced vitrimer composites: overview and future prospects. RSC Adv 2022;12:32569–82.
[34] Park JS, Kim HS, Hahn T. Healing behavior of a matrix crack on a carbon fiber/mendomer composite. Compos Sci Technol 2009;69:1082–7.
[35] Hostettler N, Cohades A, Michaud V. Statistical fatigue investigation and failure prediction of a healable composite system. Front Mater 2020;7:561852.
[36] Bodiuzzaman J, Roy S, Mulani SB. Fracture resistance of in-situ healed CFRP composite using thermoplastic healants. Mater Today Commun 2020;24:101067.
[37] Hayes SA, Jones FR, Marshiya K, Zhang W. A self-healing thermosetting composite material. Composites A 2007;38(4):1116–20.
[38] Cohades A, Michaud V. Thermal mending in E-glass reinforced poly(ϵ-caprolactone)/epoxy blends. Composites A 2017;99:129–38.
[39] Pingkarawat K, Dell'Olio C, Varley RJ, Mouritz AP. Poly(ethylene- co -methacrylic acid) (EMAA) as an efficient healing agent for high performance epoxy networks using diglycidyl ether of bisphenol a (DGEBA). Polymer 2016;92:153–63.
[40] Meure S, Wu D-Y, Furman SA. FTIR study of bonding between a thermoplastic healing agent and a mendable epoxy resin. Vib Spectrosc 2010;52(1):10–5.
[41] Turicek JS, Snyder AD, Nakshatrala KB, Patrick JF. Topological effects of 3D-printed copolymer interlayers on toughening and in situ self-healing in laminated fiber-composites. Compos Sci Technol 2023;240:110073.
[42] Meure S, Varley RJ, Wu DY, Mayo S, Nairn K, Furman S. Confirmation of the healing mechanism in a mendable EMAA–epoxy resin. Eur Polym J 2012;48(3):524–31.
[43] Pingkarawat K, Wang CH, Varley RJ, Mouritz AP. Self-healing of delamination cracks in mendable epoxy matrix laminates using poly[ethylene-co-(methacrylic acid)] thermoplastic. Composites A 2012;43(8):1301–7.
[44] Pingkarawat K, Bhat T, Craze DA, Wang CH, Varley RJ, Mouritz AP. Healing of carbon fibre–epoxy composites using thermoplastic additives. Polym Chem 2013;4(18):5007.
[45] Peñas-Caballero M, Chemello E, Grande AM, Santana MH, Verdejo R, Lopez-Manchado MA. Poly(ethylene-co-methacrylic acid) coated carbon fiber for self-healing composites. Composites A 2023;169:107537.
[46] Meure S, Furman S, Khor S. Poly[ethylene-co-(methacrylic acid)] healing agents for mendable carbon fiber laminates. Macromol Mater Eng 2010;295(5):420–4.
[47] Ladani RB, Pingkarawat K, Nguyen AT, Wang CH, Mouritz AP. Delamination toughening and healing performance of woven composites with hybrid z-fibre reinforcement. Composites A 2018;110:258–67.
[48] Loh TW, Ladani RB, Orifici A, Kandare E. Ultra-tough and in-situ repairable carbon/epoxy composite with EMAA. Composites A 2021;143:106206.
[49] Snyder AD, Phillips ZJ, Turicek JS, Diesendruck CE, Nakshatrala KB, Patrick JF. Prolonged in situ self-healing in structural composites via thermo-reversible entanglement. Nature Commun 2022;13:1–12.
[50] Hirasawa E, Yamamoto Y, Tadano K, Yano S. Formation of ionic crystallites and its effect on the modulus of ethylene ionomers. Macromolecules 1989;22(6):2776–80.
[51] Kutsumizu S, Tadano K, Matsuda Y, Goto M, Tachino H, Hara H, et al. Investigation of microphase separation and thermal properties of noncrystalline ethylene ionomers. 2. IR, DSC, and dielectric characterization. Macromolecules 2000;33(24):9044–53.
[52] Kalista SJ, Pflug JR, Varley RJ. Effect of ionic content on ballistic self-healing in EMAA copolymers and ionomers. Polym Chem 2013;4(18):4910.
[53] Francesconi A, Giacomuzzo C, Grande A, Mudric T, Zaccariotto M, Etemadi E, et al. Comparison of self-healing ionomer to aluminium-alloy bumpers for protecting spacecraft equipment from space debris impacts. Adv Space Res 2013;51(5):930–40.
[54] Grande AM, Castelnovo L, Landro LD, Giacomuzzo C, Francesconi A, Rahman MA. Rate-dependent self-healing behavior of an ethylene-co-methacrylic acid ionomer under high-energy impact conditions. J Appl Polym Sci 2013;130(3):1949–58.
[55] Varley RJ, Shen S, van der Zwaag S. The effect of cluster plasticisation on the self healing behaviour of ionomers. Polymer 2010;51(3):679–86.
[56] DuPont Inc. Technical data: Dupont™ nucrel™ 2940 ethylene-methacrylic acid copolymer resin. 2010.
[57] DuPont Inc. Technical data: Dupont™ nucrel 960™ acid copolymer. 2019.
[58] DuPont Inc. Technical data: Dupont™ surlyn™ 1702. 2014.
[59] DuPont Inc. Technical data: Dupont™ surlyn™ PC-2200. 2015.
[60] Wegst UG, Bai H, Saiz E, Tomsia AP, Ritchie RO. Bioinspired structural materials. Nature Mater 2015;14(1):23–36.
[61] Luo J-J, Daniel IM. Sublaminate-based lamination theory and symmetry properties of textile composite laminates. Composites B 2004;35(6):483–96.
[62] The Gorilla Glue Co. Technical data: Gorilla glue. 2007.
[63] ASTM E1640: Standard Test Method for Assignment of the Glass Transition Temperature By Dynamic Mechanical Analysis. ASTM International; 2018.
[64] ASTM D5528: Standard Test Method for Mode I Interlaminar Fracture Toughness of Unidirectional Fiber-Reinforced Polymer Matrix Composites. ASTM International; 2018.

[65] Hashemi S, Kinloch AJ, Williams JG. Corrections needed in double-cantilever beam tests for assessing the interlaminar failure of fibre-composites. J Mater Sci Lett 1989;8:125–9.
[66] Krull B, Patrick J, Hart K, White S, Sottos N. Automatic optical crack tracking for double cantilever beam specimens. Exp Tech 2015;40:937–45.
[67] Gurney C, Hunt J. Quasi-static crack propagation. Proc R Soc Lond A 1967;299(1459):508–24.
[68] Rivas BL, Villegas S, Ruf B. Synthesis of water-insoluble functional copolymers containing amide, amine, and carboxylic acid groups and their metal-ion-uptake properties. J Appl Polym Sci 2006;102(6):5232–9.
[69] Nazarov A, Thierry D, Volovitch P, Ogle K. An SKP and EIS investigation of amine adsorption on zinc oxide surfaces. Surf Interface Anal 2011;43(10):1286–98.
[70] Steinke K, Sodano HA. Enhanced interfacial shear strength in ultra-high molecular weight polyethylene epoxy composites through a zinc oxide nanowire interphase. Compos Sci Technol 2022;219:109218.